MDPI

Article

Open Porous Composite Monoliths for Biomedical Applications via Photocrosslinking of Low Internal Phase Nano-Emulsion Templates

Maurizio Celentano [1,2,3,*] , Raffaele Vecchione [1,2,*] , Maddalena De Simone [1,2], Eliana Esposito [1,2], Monica Patrone [1,2] and Paolo Antonio Netti [1,2]

1   Istituto Italiano di Tecnologia, IIT@CRIB, Largo Barsanti e Matteucci, 53, 80125 Napoli, Italy; marlene-1@hotmail.it (M.D.S.); eliana.esposito@live.it (E.E.); monicapat@gotmail.it (M.P.); paolo.netti@iit.it (P.A.N.)
2   Centro di Ricerca Interdipartimentale sui Biomateriali CRIB, Universitá di Napoli Federico II, Piazzale Tecchio, 80, 80125 Napoli, Italy
3   Queen's School of Chemistry and Chemical Engineering, University Belfast, 39-123 Stranmillis Rd, Belfast BT9 5AG, UK
*   Correspondence: m.celentano@qub.ac.uk (M.C.); raffaele.vecchione@iit.it (R.V.)

Abstract: Highly cross-linked polyethylene glycol monoliths (HCPEG) with interconnected micro and nanoporosity are produced via photo-crosslinking of low internal phase emulsions (LIPE). Unlike previous works, this approach allows the pre-processing functionalization of both polymer matrix and porosity by loading both phases of the emulsion template with several active fillers, such as enzymes, semiconductive polymers, and metallic nanostructures. Importantly, both polymer matrix and porosity of the resulting composite HCPEG monoliths show neither serious cross-contamination nor morphological alterations. All in all, this material behaves like a network of nano/micro flasks embedded into a permeable media. Mechanical and dielectric properties of these composites HCPEG monoliths can be tuned by varying the content of fillers. Since these composite materials are produced by photo-crosslinking of LIPEs, they can be easily and rapidly processed into complex shapes like microneedles arrays through replica molding without detrimental modifications of the porous morphology. In principle, the proposed strategy allows us to fabricate medical devices. As proof of concept, we embedded glucose oxidase enzyme in the nanoporosity and the resulting composite porous material retained the catalytic activity towards the oxidation of glucose.

Keywords: nano-porous materials; nano-emulsion templates; nanostructures; medical devices

1. Introduction

Imparting porous architecture to macroscopic objects has been a key scientific subject for a long time [1–4]. From then on, a plethora of porous materials have been synthesized and, among the others, polymer-based porous materials have gained much interest due to their easy processability and diversity of synthetic routes at our disposal [3,4]. In addition, porous polymer materials have found many applications in several fields, e.g., gas storage and separation, controlled release of drugs, catalysis, and sensing [4–7]. One subclass of porous polymer materials, known as monolithic polymer materials, is particularly promising due to some remarkable characteristics, i.e., variety of porosity, pore size, and many combinations of chemical functionalities by controlling precursors and chemistry during polymerization [8–18].

Porous polymer monoliths are usually defined as rigid and continuous objects with an open cellular porous structure, which allows fluids to flow through. These are usually prepared by copolymerization of functional monomers and crosslinkers in presence of porogenic solvents/agents. Although this approach is proven solid and feasible, it still has some limitations once a multi-functional porous polymer monolith has to be prepared.

Indeed, such functionalities are typically obtained starting from functional monomers whose functional groups are mainly lost within the dense polymer structure. Conversely, post-modification strategies of monolithics have been invoked to overcome these limitations, including post-processing chemical modification of monoliths such as epoxy groups of polymerized glycidyl methacrylate units [19,20] or modification of the pore surface by grafting of functional polymer chains [21–27]. Albeit these approaches enable independent control over porous structure and surface chemistry, they require a complex post processing modification, which in turn requires a certain degree of control over the reaction conditions, making the process not very straightforward.

On the other hand, the photoinitiated polymerization route towards porous polymer structures has been implemented in several studies [28–33] where high internal phase emulsions were used as templates. Although using high internal phase emulsions brings several sought-after structural properties, such as high porosity and degree of pores interconnectivity, it also shows some drawbacks, such as poor mechanical strength and, more importantly, the polymer structure mainly acts as a support or scaffold for post-processing functionalization.

Differently, this paper investigates the photoinitiated polymerization of low internal phase emulsion into porous monolithic materials featuring (i) interconnected meso-porosity, (ii) suitable Young' module, (iii) independent loading of the pores and polymer matrix without serious cross-contamination (controlled differential loading) with virtually any compatible materials of choice (polymers, nanostructures, biomolecules), and (iv) good processability.

Monolithic porous materials in the shape of microneedles arrays have been the subject of intense research as transdermal drug delivery systems [34–38]. On the contrary, much less attention has been paid to their application as transdermal medical devices for personal healthcare monitoring [39–41]. The skin interstitial fluid shows a dynamic exchange of molecules with capillary blood vessels therefore it allows us to access a range of analytes in a continuous and mini-invasive manner [42]. For instance, the continuous measurement of the glucose levels present in the skin interstitial fluid may allow the continuous and mini-invasive monitoring of glycaemia in diabetic patients [43]. Bearing this in mind, we have tested the proposed procedure on the fabrication of microneedles arrays by replica molding and application in glucose monitoring.

2. Materials and Methods

PEG-DA (250 Da), Pluronic F68, camphorsulfonic acid (CSA), aniline hydrochloride, ammonium persulfate $(NH_4)_2S_2O_8$ (APS), chloroauric acid, sodium citrate, glucose oxidase enzyme (GOX), D-glucose, horseradish peroxidase (HRP), Phosphate-buffered saline tablets (PBS), N,N-Diethylaniline-4-Aminoantipyrine, dimethyl carbonate (DMC), and hydrogen peroxide (30% vol) were purchased from Sigma Aldrich, photoinitiator darocure 1173 from Ciba and QUETOL 651 resin from Electron Microscopy Sciences.

2.1. Synthesis of the Loaded and Empty Porous HCPEG Monoliths and of Non Porous HCPEG Monoliths

Empty porous HCPEG monoliths and porous HCPEG monoliths loaded with fillers, such as polyaniline doped with camphorsulfonic acid (PANI), gold nanowires networks (GNWs), and glucose oxidase enzyme (GOX), were composed of highly crosslinked polyethylene glycol (HCPEG) solid specimens obtained by photo-induced radical polymerization of low internal phase emulsion templates. In these low internal phase emulsion templates, water droplets (20% vol), which could be either loaded or not loaded with fillers such as GOX and GNWs, were stabilized by the surfactant Pluronic F68 (180 mg/mL) and dispersed in the PEG-DA oil phase (80% vol), which contained the photo initiator Darocour 1173 (2% wt) and could be loaded or not loaded with PANI. Soon after being prepared, the low internal phase emulsion templates were ultrasonicated with QSONICA sonicator using a microtip (diameter 2 mm) for 20 s at amplitude 30% (6 μm) corresponding to a power density of 34 W/cm^2. The ultrasonication was carried in an ice bath to

disperse the excessive heat generated by ultrasonic waves. A few drops of low internal phase emulsion template were placed on a microscope slide, with glass spacers for each side, and covered with a coverslip. Each single glass spacer was 0.17 mm thick and the overall specimens' thickness could be modulated by varying the number of glass spacers. The photo-polymerization was then conducted on this set-up by irradiating at 365 nm with a UV lamp (Spectroline ENF-260C/FE) for 20 min to have a solid porous matrix. Once these low internal phase emulsion templates were photo-crosslinked they turned into rigid porous monolithic HCPEG (schematic representation of the fabrication process is reported in Figure 1a). Similarly, non-porous HCPEG monoliths were produced by UV photoreticolation of PEG-DA with Darocour 1173 (2% wt).
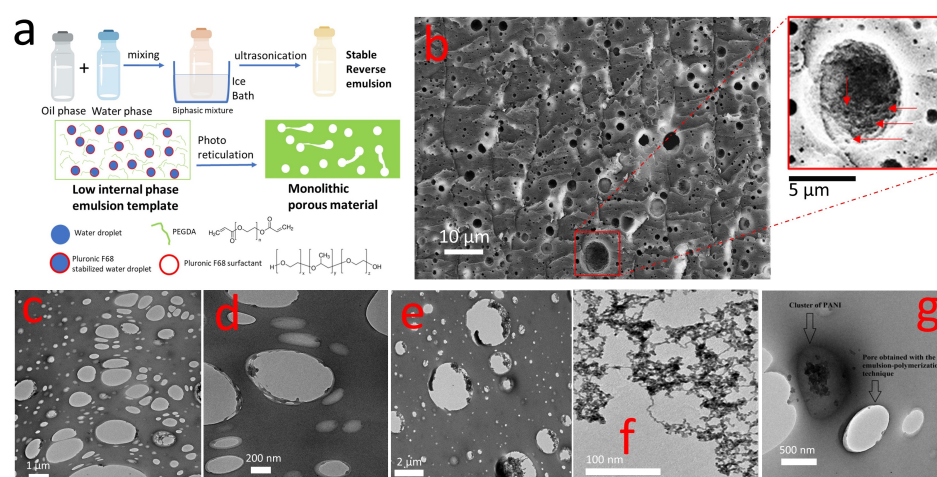
Figure 1. Schematic (**a**) of the fabrication process (Ciba® DAROCUR® 1173 photoinitiator is not represented for sake of simplicity); SEM (**b**) and TEM (**c,d**) images showing the internal structure of porous PEG (TEM scale bars 1 um (**c**) and 200 nm (**d**), SEM scale bar 10 um, the red arrows indicate the nanopores present on the walls of a microporous); (**e**) TEM image showing selective inclusion of GNWs (0.4% wt) into the pores and (**f**) a representative TEM image of the GNWs for comparison; (**g**) selective dispersion of PANI 0.8 wt % in the PEG matrix.

2.2. Synthesis of Polyaniline Doped with Camphorsulfonic Acid

Polyaniline doped with camphorsulfonic acid (PANI) was synthesized via in situ emulsion polymerization [44]. In a typical synthesis, 0.003 mol (0.704 g) of CSA was mixed with 0.05 mol (4.5 g) of aniline monomer in 200 mL of DI water for 2 h. The mixture was cooled to 273 K in an ice bath, then 50 mL of an aqueous solution containing 0.04 mol (9 g) of APS was added dropwise into the emulsion while stirring at 273 K. After 4 h, the precipitate was collected on a Buchner funnel and repeatedly rinsed with water. The products were then dried in an oven for 12 h. The final polymer was characterized by UV-visible spectroscopy, IR, and Scanning Electron Microscopy (data not showed).

2.3. Synthesis of Gold-Nanowires Networks

Gold-nanowires networks were synthesized following the procedure in [45]. Briefly, the process involved only mixing trisodium citrate (38.8 mM) and gold chloride (4 mM) stock solutions at a molar ratio R = 9.7 followed by the ageing of solution. After initial mixing the colour for all the solutions gradually changed in the following order—light yellow, colourless, reddish-black, reddish-brown, and finally to different shades of black (nanowire networks). NWNs were obtained as intermediates and a washing step with Milli-Q water was required to halt the reduction process around 2–3 h after mixing of reagents.

2.4. Solutions Preparation

Pluronic F68 standard solution was produced by dissolving 3.60 g of Plutonic F68 in 10 mL of DI water under continuous magnetic stirring. The as-produced solution was

sonicated at 59 kHz for 30 min at 313 K to ensure the complete dissolution of Plutonic F68. This stock solution was diluted with 10 mL of DI water to obtain a final concentration of 180 mg/mL in Pluronic F68 before being added to PEG-DA phase. Solution of GNWs at different concentrations were prepared by settling down the GNWs by centrifugation followed by solvent DI water removal. Final concentrations in gold(III) ions were determined by ICP-MS. Since enzyme activity is sensible to pH we buffered the water phase with PBS 100 mM at pH 7.4 when GOX (1 U/mL) was used and for the catalytic activity test. Dispersions of PANI at several % wt in PEG-DA (Table S1) were prepared following a process aided by a co-solvent (DCM). The desired amount of PANI was added to a mixture of PEG-DA and DCM 90:10 in volume, followed by sonication and evaporation of the co-solvent, after that the photo-initiator Darocur 1173 was added (2% wt).

2.5. Porous HCPEG Loading

Porous HCPEG was loaded with several materials and compounds by simply using the solutions or dispersion reported in the section above to prepare the low internal phase emulsion templates.

2.6. Electron Microscopy Analysis

Morphological characterizations were carried out by Transmission Electron Microscopy (FEI Tecnai G2 transmission electron microscope at 200 kV and images were acquired by Eagle 2K CCD-HS camera) and Scanning Electron Microscopy (Ultra Plus Zeiss Germany, FEG-SEM). TEM and SEM images were post-processed using the software Fiji. [46] For SEM and TEM analyses, small pieces of materials were immersed in QUETOL 651 resin (Electron Microscopy Sciences) for two days and were stored in a refrigerator. On the third day, the specimens were taken from the refrigerator and placed in silicon molds and a thin layer of resin was deposed on top and left to harden for more than four hours in an oven at 333 K to obtain small resin blocks with embedded specimens. These blocks were then covered with other resin and left to harden over-night at room temperature. Slices 5 μm and 50 nm thick were cut off for the SEM and TEM analyses, respectively, using a Leica CryoUlta Microtome EM-FC7-UC7.

2.7. Nanoindenter Mechanical Characterization

Mechanical characterization of composite monolithic porous materials was carried out using the nanoindenter (G200, Agilent Technologies). Thin flat films of these materials (diameter 1 cm, thickness 300 μm) were glued on stubs and were tested with Nanoindenter. The Young's modulus against the indentation depth was recorded for each sample and calculated as the value corresponding to the establishment of the plateau. Setting parameters were: Depth Limit 6000 nm; Strain Rate Target 0.05 1/s; Harmonic Displacement Target 2 nm; Frequency Target 40 Hz; Poisson Ratio 0.33; Surface Approach Velocity 30 nm/s; Surface Approach Distance 5000 nm; Max Profundity Depth 6000 nm.

2.8. Confocal Fluorescence Microscopy Characterization

Permeability tests were conducted by observing the penetration of sulforhodamine B, both in porous HCPEG and in non-porous HCPEG. Thin films were prepared following the subsequent procedure: one drop (20 uL) of prepolymer solution was deposited on a sheet of non-adhesive transparent teflon, then covered with another sheet of transparent teflon and squeezed between using a weight. These sandwiches were exposed to UV light (at 365 nm wavelengths for 20 min) to photo-reticulate. The thicknesses of the layers were evaluated using the profilometer (VEECO DEKTAT 150). The range of thickness was measured between 40–60 μm. The as-produced specimens were shaped into 5 by 5 mm square and then immersed into 1 mL sulforhodamine B (1 mg/mL) solution for a specified period. The specimens were recovered and left to dry before being included in a PDMS block. In a mold for material inclusion in resin, a first layer of PDMS was deposed and cured at 90 °C. On this layer, the recovered and dried specimens were covered with another
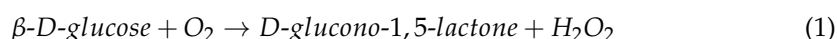
PDMS layer. When the block of PDMS was hardened, 5 μm slices of these specimens in PDMS were achieved by using a Leica CryoUlta Microtome EM-FC7-UC7. The sectioning was carried out at T $\sim$ 88 K which is far below the glass transition temperature of PDMS polymer (Tg $\sim$ 152 K). Due to the low temperature employed during the process the specimens were easier to slice but also brittle bringing to some variability between different slices. Slices coming as much as possible from a similar region of different specimens were selected and observed at the confocal (LEICA TCS SP5II) with excitation laser set at 543 nm wavelengths.
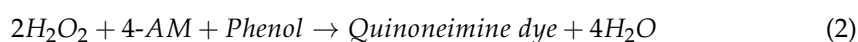
2.9. Impedance Spectroscopy Analysis

AC electrical response of the composites was investigated through Impedance Spectroscopy Analysis using a two-probe method formed by two aluminum discs as electrodes connected to an AUTOLAB PGSTAT302N (potentiostat/galvanostat) equipped with a FRA32M module (frequency response analysis module). Impedance spectra were recorded in potentiostatic mode with an amplitude of 0.01 V and frequencies ranging from 100 kHz to 0.01 Hz between the electrodes. For each measurement, three readings and 50 data points (logarithmic frequency step) per reading were collected.

2.10. Enzymatic Activity Analysis

The enzymatic activity of GOX pristine and in the porous materials was validated at room temperature by colorimetry of N,N-Diethylaniline-4-Aminoantipyrine (4-AM) [32]. The assay is based on the following reactions:
reaction catalyzed by GOX

$$\beta\text{-}D\text{-}glucose + O_2 \rightarrow D\text{-}glucono\text{-}1,5\text{-}lactone + H_2O_2 \tag{1}$$

reaction catalyzed by HRP

$$2H_2O_2 + 4\text{-}AM + Phenol \rightarrow Quinoneimine\ dye + 4H_2O \tag{2}$$

GOX, and monolith with GOX were, separately, put in contact with a PBS (100 mM) solution of phenol (0.01 M), 4-AM (2.2 mM) and β-D-glucose (0.1 M), and HRP (1.25 U/mL). In both cases, GOX concentration was Units/mL. Change in the absorbance at 500 nm of the solution indicates the generation of Quinoneimine dye, which on its turn indicates the generation of hydrogen peroxide due to the β-D-glucose oxidation to D-glucono-1,5-lactone that is catalyzed by the GOX enzyme.

3. Results and Discussion

As it will be shown later in this manuscript, using LIPEs as templates gave access to a high degree of versatility in terms of formulations and functionalization. As with any other emulsion, LIPE is made of two immiscible phases that can be possibly loaded by any compatible fillers. Therefore, functionalities can be imparted to the polymer matrix and the porosity in a specific and selective way. (The high volume and mass fraction of the oil phase makes possible a high relative loading of the polymer matrix generated by conversion of the LIPE into porous HCPEG via photopolymerization. This level of loading would not be achievable in the case of a high internal phase emulsion due to the reduced volume of the oil phase.

As anticipated previously, the material processability was investigated and tested towards several runs of microneedles arrays fabrication by replica molding, the main aspects of which will be later discussed more in detail.

In order to fabricate practical microneedles arrays, the formulation of the low internal phase emulsion was optimized to reach the best compromise between mechanical strength and porosity once photo-crosslinked into a monolithic porous polymer material. Ideally, the Young's Modulus of a microneedle should be 1.0 GPa or more to enable skin piercing [47]. On the other hand, the presence of open and dense porosity was also desirable

from many applicative standpoints, e.g., microneedles patch for drug delivery, body fluids suction, and bio-sensing devices. Eventually, we optimized a material featuring dense meso-porosity without compromising the mechanical performance in respect to the bulk plastic material. SEM morphological analysis (Figure 1b) of our porous HCPEG showed an inner porosity composed of several sub-micrometric pores randomly distributed throughout the material. Nevertheless, a closer look at the material by means of TEM morphological analysis (Figure 1c,d) clearly revealed nano-pores throughout the inner structure.

It was evident from the morphological analysis that this material featured micro and nano-porosities. Nanoindentation mechanical characterizations of both porous and non-porous HCPEG showed a decrease in Young's Modulus from 2.16 GPa down to 1.63 GPa (Figure 2) because of the porous inner structure. Despite this remarkable decrease, the Young's Modulus was still well above the 1.0 GPa threshold. Notably, the Young's Modulus did not scatter throughout all the indentation depth, indicating that the porosity was homogenous throughout the inner structure of porous-PEG on the nanoindenter length scale.
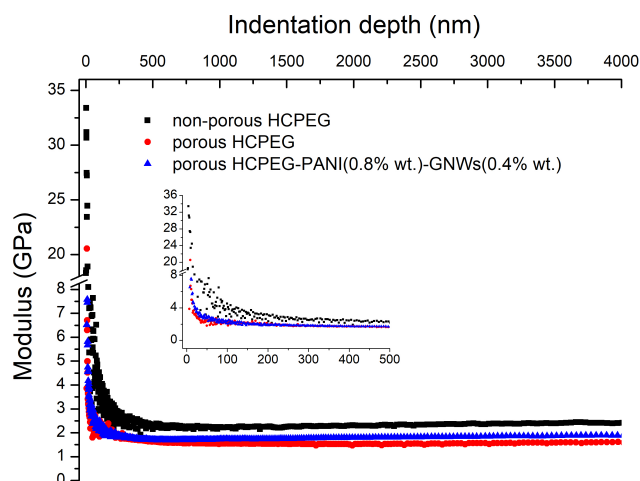
Figure 2. Nanoindentation experiments showing the Young's Modulus (GPa) as a function of the indentation depth HCPEG, porous HCPEG, and porous HCPEG filled with PANI (0.8% wt) (c) and PANI (0.8% in wt) plus GNWs (0.4% wt).

So far, we have achieved a material showing mechanical strength, micro, and nano-porosity. A closer inspection of the porosity by SEM (Figure 1b) shows mesopores sitting on the walls of micropores (indicated by the red arrows in the insert). Seemingly, the morphological analysis indicated an open porous structure.

Following this conclusion, we further tested it by carrying out molecular permeability studies. Specimens of the monolithic material (porous and non-porous) were immersed in sulforhodamine B solutions and their inner structures were afterward observed with confocal fluorescence microscopy (Figure 3a–c). Notably, the fluorescence signal coming from the probe molecules was found to be evenly distributed in the porosity throughout the material. At the same time, the bulk non-porous plastic material did not allow probe fluorescent molecules to penetrate the inner structure (Figure 3a). It is obvious that in presence of a closed porous structure the fluorescent probe molecules must be found just in proximity of the specimen surface, as it happens for the bulk non-porous material. Nevertheless, the fluorescent probe can be found in the internal pores of the specimen only if the pores are somehow interconnected and molecules can freely move throughout the material. On this basis, we deduced that molecules may permeate throughout the polymer mesh with the pores acting as micro/nano-flasks.
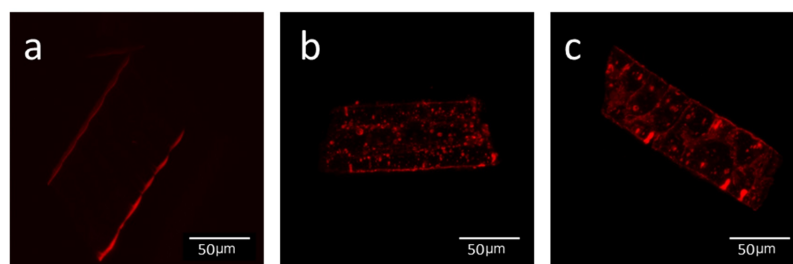
Figure 3. Confocal Fluorescence Microscopy of the internal of a non-porous HCPEG (**a**) and of a porous HCPEG matrix taken 5 min (**b**) and 30 min (**c**) after immersion in sulforhodamine B solution (1 mg/mL). The red color indicates the sulforhodamine B.

As proof of concept of phase-specific loading, we first loaded the oil phase with polyaniline emeraldine salt doped by camphorsulfonic acid (PANI), and the pores with gold nanowires networks (GNWs). Polyaniline emeraldine salt is a semiconductive polymer featuring many advantages over other semiconducting polymers such as low cost, easy synthesis, range of electrical conductivities, and unique reversible proton doping/de-doping processes [48]. The semi-conductiv emeraldine salt form of polyaniline features a partially filled valence band, which makes it electrically semiconductive via hopping of delocalized radical polaron. This condition makes this polymer highly polarizable and its polarizability depends on the valence band filling density. The polarizability of polyaniline determines its impedance response, and it can be tuned by modifying the radical polaron distribution through structural or chemical changes in the polymer chain. Despite its advantages, polyaniline is not easy to process because it is poorly dispersed in water and most organic solvents. Despite this, we found out that polyaniline doped CSA is easily dispersible in the low internal phase emulsion up to 0.8% wt.

On the other hand, gold nanowires networks (GNWs) are 2D plasmonic nanostructures dispersed in water. These metallic nanostructures show catalytic activity, can be easily functionalized with biomolecules, and can serve as SERS substrates [45]. Furthermore, both fillers do not significantly affect the indentation profile (Figure 2). The thickness of the nanowires in the GNWs can vary from 4–5 nm to a few tens of nm and the extension of the network can reach several microns. The percentage of gold was 0.4% wt and it was the highest amount possible.

Electron microscopy (TEM and SEM) of the composite materials gave insights into ultrastructure. Despite the loading of fillers in the phases composing the low internal phase emulsion, the composite materials retained the porous morphology (Figure 1e,g). Moreover, TEM and SEM analysis pointed out that each filler was included in specific regions, indeed GNWs were mostly included in the pores (Figure 1e), while polyaniline was dispersed in the HCPEG matrix (Figure 1g). Thus, phase selective loading of pores and polymer matrix could be achieved using this procedure. This selectivity is explained by considering that polyaniline is dispersible in PEG-DA but immiscible with water; instead, gold nanowires networks are dispersible in water and immiscible with PEG-DA. Moreover, during the preparation of the low internal phase emulsion, there is no contamination of the porosity with PANI although Au signals can be found both in the porosity and in the polymer matrix (Figure S1). Figure 1f shows a TEM image of GNWs which well compares to the GNWs included in the pores (Figure 1e). Statistical descriptors (Table 1) indicate that by increasing the loading of PANI in the porous HCPEG the porosity distribution shifts towards larger sizes and it becomes more dispersed.

Table 1. Average pores sizes and standard deviations of the several materials (avg. stands for average, s.d. for standard deviation).

Specimen	avg. Diameter, μm	s.d.
HCPEG	0.77	2.21
HCPEG + GNW(0.4% wt)	0.25	0.56
HCPEG + PANI(0.01% wt)	1.69	2.16
HCPEG + PANI(0.05% wt)	2.11	2.79
HCPEG + PANI(0.1% wt)	2.36	3.07
HCPEG + PANI(0.8% wt)	3.16	4.25

Besides this, the effect of the GNWs filling on the pore size distribution was considered (Figure S2) and the higher was the concentration of GNWs the smaller and more uniform was the porosity. This effect recalls what is generally observed in Pickering emulsions [49] where nanostructures, due to their good wettability both in the oil and water phases, absorb on the droplets surface to form a coating to prevent them from gathering. In Figure 1e the nanostructures were localized at the edges of the pore, which once was the interface between oil and water phases. This morphological feature is a strong indication of the Pickering effect.

Dielectric properties of several composite materials were investigated by Electrical Impedance Spectroscopy (ESI). Nyquist Plots (Z' vs. –Z'' plots), Impedance vs. frequency, and Phase shift vs. frequency plots, also known as Bode Plots, are reported in Figure 4 for the following porous monoliths: HCPEG (Figure 4a,b), HCPEG−GNWs (0.4% wt) (Figure 4c,d), HCPEG−PANI (0.8% wt) (Figure 4e,f), and HCPEG−PANI (0.8% wt)−GNWs (0.4% wt) (Figure 4g,h). All the monoliths showed two characteristic time constants (τ_1 and τ_2, two distorted semi-circles in the Nyquist plots) indicating the existence of two dipole relaxation processes.

Nyquist plots showed a certain degree of distortion indicating that the frequency-dependent impedance cannot be interpreted in terms of ideal circuit elements in an equivalent circuit. Besides, we may tentatively ascribe these two processes to the dipole relaxation of the polymer matrix and porosity respectively, but it is difficult, if not impossible, to derive physical parameters like a chemical capacity, a double layer capacity, or a resistance which can be linked either to one phase or the other just by fitting an equivalent circuit. These physical parameters are lumped and cannot be derived directly.

Surely, both fillers (PANI and GNWs) had a profound impact on the time constants τ_1 and τ_2 by decreasing their values which means faster dipole relaxation processes. Bode plots of porous monolithic HCPEG and HCPEG−GNWs (0.4% wt) (Figure 4b,d) showed high impedance at low frequency at about −90 phase angle (ϕ), clearly indicating a capacitive behaviour. When the frequency increased, the phase angle (ϕ) dropped to around −20 and −12 phase angle (ϕ) which was at around 1.9 Hz and 5.2 Hz, respectively, then it started increasing again. This suggests the occurrence of a transition from capacitive to a resistive behaviour via a dipole relaxation at those frequencies. By adding GNWs to the porous phase the resonance of this dipole relaxation shifted towards a higher frequency. Owing to that GNWs uniquely fill the porosity, one may claim that this dipole relaxation was mainly associated with the porosity.
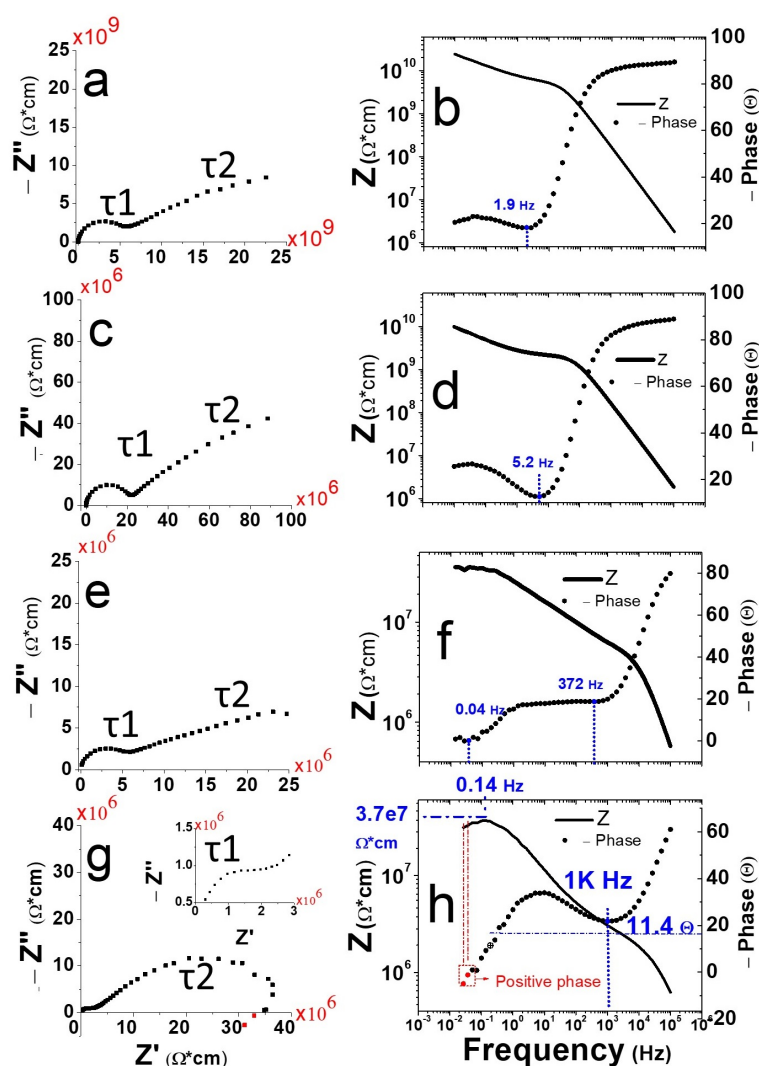
Figure 4. Impedance analysis of pristine porous HCPEG monolithic specimens (**a**,**b**) and porous HCPEG monolithic loaded with: GNWs (0.4% wt). (**c**,**d**), PANI (0.8% wt) (**e**,**f**) and PANI (0.8% wt) + GNWs (0.4% wt) (**g**,**h**).

When it comes to the HCPEG−PANI (0.8% wt), two resonances at low and at high frequencies were noticed (0.04 and 372 Hz, Figure 4e,f). Being PANI the most abundant filler, the evidence that it affected the dielectric properties, to a major extent compared to the sole GNWs, was expected.

The high-frequency dipole relaxation resonance was likely due mainly to the PANI, which filled the HCPEG matrix. Moreover, to some extent, it also influenced the dipole dielectric relaxation due to the pores.

In HCPEG−PANI (0.8% wt)−GNWs (0.4% wt) (Figure 4g,h) the low-frequency resonance almost faded away. This can be explained by invoking some sort of synergic effect where PANI and GNWs together furtherly shift this dipole relaxation towards lower frequencies, beyond the frequency range of the ESI analysis.

Notably, the Nyquist plot for HCPEG−PANI (0.8% wt)−GNWs (0.4% wt) showed a low frequency hook ending in the positive Z″ quadrant (Figure 4g,h red marks). A positive phase angle impedance indicates that current lags voltage in the frequency range. This feature may be the signature of an inductive behaviour where energy is stored as a magnetic field, albeit it is our opinion that this is unreasonable due to the excessive and incredibly large corresponding inductance. On the other hand, assigning the low-frequency hook to a negative capacitance is even more unrealistic.
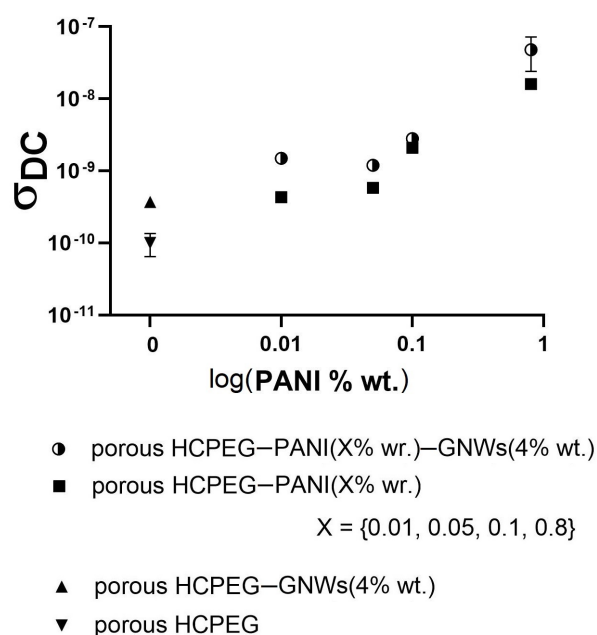
More reasonably, the low-frequency hook comes from the entanglement or reciprocal interaction between the PANI, which is dispersed in the polymer matrix, and the porosity, which is partially filled with GNWs.

AC conductivities of these composites were obtained from the dielectric losses measured as a function of pulsation [50] according to Equation (3):

$$\sigma_{AC}(\omega) = \epsilon_0 \omega \epsilon'' \tag{3}$$

Then the DC conductivities (Figure 5) were obtained by applying Jonscher's power law [51] in Equation (4):

$$\sigma_{AC}(\omega) = \sigma_{DC} + K\omega^s \tag{4}$$

◑ porous HCPEG−PANI(X% wr.)−GNWs(4% wt.)
■ porous HCPEG−PANI(X% wr.)

X = {0.01, 0.05, 0.1, 0.8}
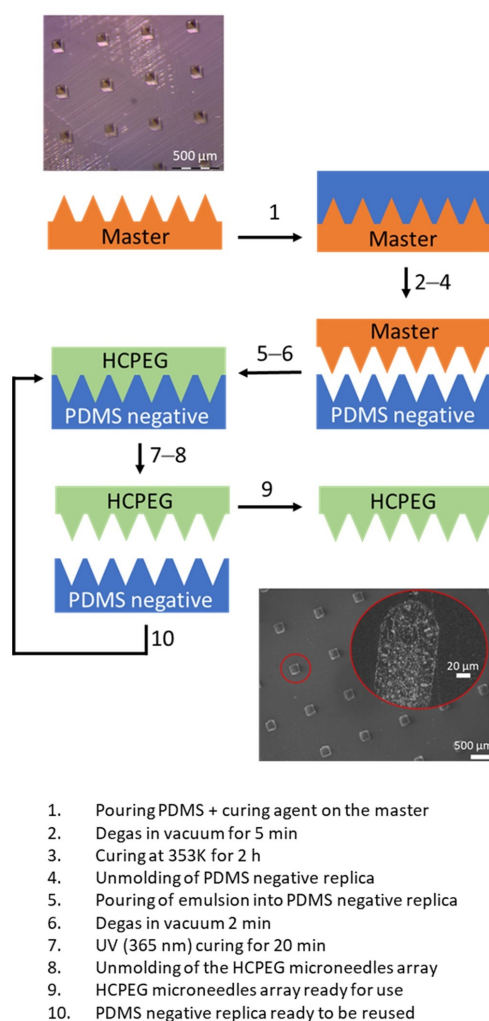
▲ porous HCPEG−GNWs(4% wt.)
▼ porous HCPEG

Figure 5. DC conductivity of the composite materials with inner porous structure.

For the production of mixed matrices, i.e., containing both fillers, it was decided to use GNW at the highest concentration (0.4% wt) for each specimen as it offers the best results in terms of porosity, and to vary only the contents of PANI. As expected electrical and dielectric properties are strongly influenced by the addition of fillers.

PEG porous matrix exhibited a typical insulating behavior characterized by low DC conductivity. By adding PANI, a semiconductive polymer, the DC conductivity increased as the filler content was increased, and a further increase occurs when GNWs are also present. The processability of the porous plastic material was tested against several runs of microneedles arrays replica molding (Figure 6). SEM morphological analysis shows that the material well replicates an array of microneedles by following this simple procedure. It is worth it to note that the internal porous architecture is preserved in the microneedles (Figure 6) despite the replica process.

As pointed out previously, water solutions can penetrate throughout the polymer matrix and enter the pores. These pores can act as micro/nano-flasks hosting molecules or even nanostructures. The inclusion of nanostructures represents a surplus due to the following reasons: (i) they can be firmly anchored to the pores due to their size, making impossible for them to escape into the matrix; (ii) nanostructures, can be imparted with specific functionalities to open up a wide range of applications.

1. Pouring PDMS + curing agent on the master
2. Degas in vacuum for 5 min
3. Curing at 353K for 2 h
4. Unmolding of PDMS negative replica
5. Pouring of emulsion into PDMS negative replica
6. Degas in vacuum 2 min
7. UV (365 nm) curing for 20 min
8. Unmolding of the HCPEG microneedles array
9. HCPEG microneedles array ready for use
10. PDMS negative replica ready to be reused

Figure 6. Schematic of the replica moulding fabrication process; optical image (**upper**) of the master microneedle array; SEM images (**bottom**) of the porous PEG microneedles array replica and inner structure of one single needle showing the porosity.

Overall, the pores can behave as micro/nano-reactors with a relevant chemical entity, such as a catalyst, firmly anchored inside and the proper reactant molecules can reach the pores through the polymer mesh by diffusion, feeding in this way the reaction. To test this hypothesis, we made a preliminary experiment by loading free glucose oxidase enzyme, GOX (Figure 7a,b), enzymatic activity was tested by colorimetric assay [52]. Remarkably, the monolithic porous material loaded with GOX (1 U/mL) and PANI (0.8% wt) retained the enzymatic activity towards glucose oxidation to glucanolactone (Figure 7c). Some decrease of the GOX enzymatic activity was observed likely due to a partial denaturation of the enzyme occurring during the monolith fabrication process. The colorimetric marker quinoneimine was generated by the reaction catalyzed by horseradish peroxidase (HRP) which uses the hydrogen peroxide generated and released by the pores because of the glucose oxidase (GOX) enzymatic reaction (see section Enzymatic activity analysis). Ultimately, the marker is only detected when hydrogen peroxide starts leaving the specimen to reach the solution. Accordingly, when the reaction is carried out in the pores we observed a longer induction period (Figure 7c). As proof of concept, we load the HCPEG matrix with semiconductive PANI (0.8% wt) and the porosity with either GOX or GNWs. The polarizability of PANI can be modified by radicals and peroxides which alter the density of polaron states. We observed that the dielectric properties of the HCPEG matrix are quantitatively altered by the PANI filler (Figure 4e,g). Combining this aspect with the tuneable polarizability of the polyaniline itself makes the as-proposed monolithic porous composite

a stimulus-responsive material. Conveniently, the GOX enzyme loaded into the pores can generate these stimuli which can reach the polyaniline filler thanks to the permeability of the material (Figures 3 and 6), indeed GOX is a peroxidase enzyme generating hydrogen peroxide through its catalytic cycle (Figure 7a). Furthermore, the addition of GNWs to the formulation provides several advantages, such as increased emulsion stability and improved porosity distribution (Figure S2). Moreover, GNWs could be functionalized with enzymes like GOX and homogenize the distribution of the enzyme itself throughout the porosity. It is evident that the choice we made in terms of active fillers was not casual, as well as the microneedles replica molding to test the processability. In fact, the fillers were chosen by having in mind the progression of these composites into microneedles patches for the bloodless glycaemia monitoring by piercing and suctioning fluids from the dermis. Several studies towards this direction are currently ongoing within our group. Despite the specific needs which directed the choices above, the methodology we propose in this contribution is not limited to the mentioned application but has potentialities that go beyond and cover a much wider range, like active filtering and molecular sieving, composites materials for inflow catalysis, and many others.
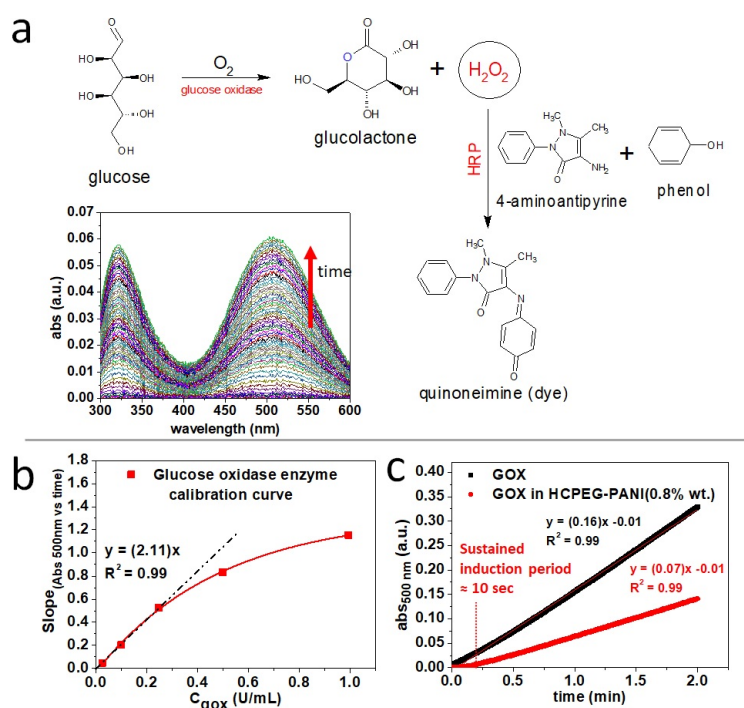
Figure 7. Porous monolithic HCPEG−PANI(8% wt) functionalized with glucose oxidase enzyme. (**a**) Colorimetric assay reaction and UV visible spectra; (**b**) glucose oxidase enzyme activity colorimetric calibration curve; (**c**) comparison between glucose oxidase enzyme activity in solution (1 Units/mL, PBS 100 mM, ph = 7.3) and embedded (1 Units/mL, PBS 100 mM, ph = 7.3) in the porous monolithic HCPEG−PANI (8% wt).

4. Conclusions

In conclusion, in this contribution we present a versatile method for the fabrication of meso-porous monolithic plastic materials by photo-reticulation of stabilized low internal phase emulsions. Morphological analysis and permeability studies indicate that the as-prepared materials have an open-porous structure where the pores are interconnected. Furthermore, the fabrication procedure here adopted allows the operator to control the loading of the pores and the polymer mesh with different active fillers without considerable cross-contamination. The active fillers were chosen by having in mind a potential furthering of these monolithic porous materials into microneedles patches for bloodless glycaemia

monitoring in the dermis. Our founding motivated further studies towards this direction which are currently ongoing within our group. Our analysis indicates that the proposed procedure enables us to easily tune several material properties, such as mechanical hardness and dielectric behavior. The great stability of the low internal phase emulsion makes it easily processable into complex shapes by photo reticulation, such as microneedles arrays. The proposed procedure is one of the most versatile and tuneable, which gives meso-porous plastic materials with considerable functionality.

References

1. Zhang, J.; Chen, J.; Peng, S.; Peng, S.; Zhang, Z.; Tong, Y.; Miller, P.W.; Yan, X.P. Emerging Porous Materials in Confined Spaces: From Chromatographic Applications to Flow Chemistry. *Chem. Soc. Rev.* **2019**, *48*, 2566–2595. [CrossRef]
2. Zhao, B.; Kumar Gain, A.; Ding, W.; Zhang, L.; Li, X.; Fu, Y. A Review on Metallic Porous Materials: Pore Formation, Mechanical Properties, and Their Applications. *Int. J. Adv. Manuf. Technol.* **2017**, *95*, 2641–2659. [CrossRef]
3. Kim, J.Y.; Yoon, S.B.; Kooli, F.; Yu, J.S. Synthesis of Highly Ordered Mesoporous Polymer Networks. *J. Mater. Chem.* **2001**, *11*, 2912–2914. [CrossRef]
4. Sadasivuni, K.; Cabibihan, J.J.; Deshmukh, K.; Goutham, S.; Abubasha, M.; Gogoi, J.; Klemenoks, I.; Sakale, G.; Sekhar, B.; Sreekanth, P.; et al. A Review on Porous Polymer Composite Materials for Multifunctional Electronic Applications. *Polym. Plast. Tech. Mat.* **2018**, *58*, 1253–1294. [CrossRef]
5. Rashidi, S.; Esfahania, J.; Rashidi, A. A Review on the Applications of Porous Materials in Solar Energy Systems. *Renew. Sust. Energ. Rev.* **2017**, *73*, 1198–1210. [CrossRef]
6. Vázquez, M.; Brett, P. Review on Recent and Advanced Applications of Monoliths and Related Porous Polymer Gels in Micro-Fluidic Devices. *Anal. Chim. Acta* **2010**, *668*, 100–113. [CrossRef] [PubMed]
7. Rashidi, S.; Kashefi, M.; Kim, C.; Samimi-Abianehd, O. Potentials of Porous Materials for Energy Management in Heat Exchangers – A Comprehensive Review. *Appl. Energy* **2019**, *243*, 206–232. [CrossRef]
8. Buchmeiser, M. Polymeric Monolithic Materials: Syntheses, Properties, Functionalization and Applications. *Polymer* **2007**, *48*, 2187–2198. [CrossRef]
9. Svec, F. Less Common Applications of Monoliths: I. Microscale Protein Mapping with Proteolytic Enzymes Immobilized on Monolithic Supports. *Electrophoresis* **2006**, *27*, 947–961. [CrossRef]
10. Svec, F. Porous Polymer Monoliths: Amazingly Wide Variety of Techniques Enabling Their Preparation. *J. Chromatogr. A* **2010**, *1217*, 902–924. [CrossRef]
11. Krenkova, J.; Svec, F. Less Common Applications of Monoliths: IV. Recent Developments in Immobilized Enzyme Reactors for Proteomics and Biotechnology. *J. Sep. Sci.* **2012**, *35*, 1266–1283. [CrossRef]
12. Tetala, K.; van Beek, T. Bioaffinity Chromatography on Monolithic Supports. *J. Sep. Sci.* **2010**, *33*, 422–438. [CrossRef] [PubMed]
13. Wistuba, D. Chiral Silica-Based Monoliths in Chromatography and Capillary Electrochromatography. *J. Chromatogr. A* **2010**, *1217*, 941–952. [CrossRef]

14. Svec, F.; Tennikova, T.B.; Deyl, Z. *Monolithic Materials: Preparation, Properties and Applications*; Elsevier: Amsterdam, The Netherlands, 2003.
15. Potter, O.; Breadmorea, M.; Hilder, E. Boronate Functionalised Polymer Monoliths for Microscale Affinity Chromatography. *Analyst* **2006**, *131*, 1094–1096. [CrossRef] [PubMed]
16. Jiang, T.; Mallik, R.; Hage, D. Affinity Monoliths for Ultrafast Immunoextraction. *Anal. Chem.* **2005**, *77*, 2362–2372. [CrossRef] [PubMed]
17. Mallik, R.; Wa, C.; Hage, D. Development of Sulfhydryl-Reactive Silica for Protein Immobilization in High-Performance Affinity Chromatography. *Anal. Chem.* **2007**, *79*, 1411–1424. [CrossRef] [PubMed]
18. Nischang, I.; Causon, T. Porous Polymer Monoliths: From Their Fundamental Structure to Analytical Engineering Applications. *Trends Analyt. Chem.* **2016**, *75*, 108–117. [CrossRef]
19. Svec, F.; Fréchet, J. Monolithic poly(2-vinyl-4,4-dimethylazlactone-co-acrylamide-co-ethylene dimethacrylate) support for design of high throughput bioreactors. *J. Chromatogr. A* **1995**, *702*, 89. [CrossRef]
20. Xie, S.; Svec, F.; Fréchet, J. Preparation of porous hydrophilic monoliths: Effect of the polymerization conditions on the porous properties of poly (acrylamide-co-N,N-methylenebisacrylamide) monolithic rods. *Polym. Prepr.* **1997**, *38*, 211–212. [CrossRef]
21. Meyer, U.; Svec, F.; Fréchet, J.M.J.; Hawker, C.J.; Irgum, K. Use of Stable Free Radicals for the Sequential Preparation and Surface Grafting of Functionalized Macroporous Monoliths. *Macromolecules* **2000**, *33*, 7769–7775. [CrossRef]
22. Viklund, C.; Nordström, A.; Irgum, K.; Svec, F.; Fréchet, J.M.J. Preparation of Porous Poly(styrene-co-divinylbenzene) Monoliths with Controlled Pore Size Distributions Initiated by Stable Free Radicals and Their Pore Surface Functionalization by Grafting. *Macromolecules* **2001**, *34*, 4361–4369. [CrossRef]
23. Rohr, T.; Hilder, E.F.; Donovan, J.J.; Svec, F.; Fréchet, J.M.J. Photografting and the control of surface chemistry in three-dimensional porous polymer monoliths. *Macromolecules* **2003**, *36*, 1677–1684. [CrossRef]
24. Peterson, D.S.; Rohr, T.; Svec, F.; Fréchet, J.M.J. Dual-Function Microanalytical Device by In Situ Photolithographic Grafting of Porous Polymer Monolith: Integrating Solid-Phase Extraction and Enzymatic Digestion for Peptide Mass Mapping. *Anal. Chem.* **2003**, *75*, 5328–5335. [CrossRef] [PubMed]
25. Pucci, V. Monolithic columns with a gradient of functionalities prepared via photoinitiated grafting for separations using capillary electrochromatography. *J. Sep. Sci.* **2004**, *27*, 779. [CrossRef]
26. Lubbad, S. A New Approach to High-Capacity Functionalized Monoliths via Post-Synthesis Grafting. *Rapid Commun.* **2003**, *24*, 580. [CrossRef]
27. Viklund, C.; Svec, F. Fast Ion-Exchange HPLC of Proteins Using Porous Poly(glycidyl methacrylate-co-ethylene dimethacrylate) Monoliths Grafted with Poly(2-acrylamido-2-methyl-1-propanesulfonic acid). *Biotechnol. Prog.* **1997**, *13*, 597. [CrossRef]
28. Kimmins, S.; Wyman, P.; Cameron, N.R. Photopolymerised methacrylate-based emulsion-templated porous polymers. *React. Funct. Polym.* **2012**, *72*, 947–995. [CrossRef]
29. Hori, K.; Sano, M.; Suzukib, M.; Hanabusa, K. Preparation of porous polymer materials using water-in-oil gel emulsions as templates. *Polym. Int.* **2018**, *67*, 909–916. [CrossRef]
30. Gokmen, M.T.; Camp, W.V.; Colver, P.J.; Bon, S.A.F.; Du Prez, F.E. Fabrication of Porous "Clickable" Polymer Beads and Rods through Generation of High Internal Phase Emulsion (HIPE) Droplets in a Simple Microfluidic Device. *Macromolecules* **2009**, *49*, 9289–9294. [CrossRef]
31. Pierre, S.J.; Thies, J.; Dureault, A.; Cameron, N.; van Hest, J.; Carette, N.; Cichin, T.; Wedberskirch, R. Covalent Enzyme Immobilization onto Photopolymerized Highly Porous Monoliths. *Adv. Mater.* **2006**, *18*, 1822–1826. [CrossRef]
32. Cummins, D.; Wyman, P.; Duxbury, C.J.; Thies, J.; Koning, C.E.; Heise, A. Synthesis of Functional Photopolymerized Macroporous PolyHIPEs by Atom Transfer Radical Polymerization Surface Grafting. *Chem. Mater.* **2007**, *19*, 5285–5292. [CrossRef]
33. Lovelady, E.; Kimmins, S.D.; Wubc, J.; Cameron, N.R. Preparation of emulsion-templated porous polymers using thiolene and thiolyne chemistry. *Polym. Chem.* **2011**, *2*, 559–562. [CrossRef]
34. Halder, J.; Gupta, S.; Kumari, R.; Gupta, G.D.; Rai, V.K. Microneedle Array: Applications, Recent Advances, and Clinical Pertinence in Transdermal Drug Delivery. *J. Pharm. Innov.* **2020**. [CrossRef] [PubMed]
35. Waghule, T.; Singhvi, G.; Dubey, S.K.; Pandey, M.M.; Gupta, G.; Singh, M.; Dua, K. Microneedles: A smart approach and increasing potential for transdermal drug delivery system. *Biomed. Pharmacother.* **2019**, *109*, 1249–1258. [CrossRef]
36. Onesto, V.; Di Natale, C.; Profeta, M.; Netti, P.A.; Vecchione, R. Engineered PLGA-PVP/VA based formulations to produce electro-drawn fast biodegradable microneedles for labile biomolecule delivery. *Prog. Biomater.* **2020**, *9*, 203–217. [CrossRef]
37. Jamaledin, R.; Makvandi, P.; Yiu, C.K.; Agarwal, T.; Vecchione, R.; Sun, W.; Maiti, T.K.; Tay, F.R.; Netti, P.A. Engineered Microneedle Patches for Controlled Release of Active Compounds: Recent Advances in Release Profile Tuning. *Adv. Ther.* **2020**, *3*, 1–27. [CrossRef]
38. Di Natale, C.; De Rosa, D.; Profeta, M.; Jamaledin, R.; Attanasio, A.; Lagreca, E.; Scognamiglio, P.L.; Netti, P.A.; Vecchione, R. Design of biodegradable bi-compartmental microneedles for the stabilization and the controlled release of the labile molecule collagenase for skin healthcare. *J. Mater. Chem. B* **2021**, *9*, 392–403. [CrossRef]
39. Esfandyarpour, R.; Esfandyarpour, H.; Javanmard, M.; Harris, J.S.; Davis, R.W. Microneedle biosensor: A method for direct label-free real time protein detection. *Sens. Actuators B Chem.* **2013**, *177*, 848–855. [CrossRef]
40. McConville, A.; Davis, J. Transdermal microneedle sensor arrays based on palladium: Polymer composites. *Electrochem. Commun.* **2016**, *72*, 162–165. [CrossRef]

41. Sharma, S.; Saeed, A.; Johnson, C.; Gadegaard, N.; Cass, A.E. Rapid, low cost prototyping of transdermal devices for personal healthcare monitoring. *Sens. Bio-Sens. Res.* **2017**, *13*, 104–108. [CrossRef]

42. Wiig, H.; Swartz, M.A. Interstitial fluid and lymph formation and transport: Physiological regulation and roles in inflammation and cancer. *Physiol. Rev.* **2012**, *92*, 1005–1060. [CrossRef]

43. Cengiz, E.; Tamborlane, W.V. A tale of two compartments: Interstitial versus blood glucose monitoring. *Diabetes Technol. Ther.* **2009**, *11*. [CrossRef]

44. Xie, D.; Jiang, Y.; Pan, W.; Li, D.; Wu, Z.; Li, Y. Fabrication and characterization of polyaniline-based gas sensor by ultra-thin film technology. *Sens. Actuators B Chem.* **2002**, *81*, 158–164. [CrossRef]

45. Jakhmola, A.; Celentano, M.; Vecchione, R.; Manikas, A.; Battista, E.; Calcagno, V.; Netti, P.A. Self-assembly of gold nanowire networks into gold foams: Production, ultrastructure and applications. *Inorg. Chem. Front.* **2017**, *4*, 1033–1041. [CrossRef]

46. Schindelin, J.; Arganda-Carreras, I.; Frise, E.; Kaynig, V.; Longair, M.; Pietzsch, T.; Preibisch, S.; Rueden, C.; Saalfeld, S.; Schmid, B.; et al. Fiji: An open-source platform for biological-image analysis. *Nat. Methods* **2012**, *9*, 676–682. [CrossRef]

47. Park, J.H.; Allen, M.G.; Prausnitz, M.R. Biodegradable polymer microneedles: Fabrication, mechanics and transdermal drug delivery. *J. Control. Release* **2005**, *104*, 51–66. [CrossRef] [PubMed]

48. Heeger, A. Nobel Lecture: Semiconducting and metallic polymers: The fourth generation of polymeric materials. *Rev. Mod. Phys.* **2001**, *73*, 681. [CrossRef]

49. Pickering, S. Emulsions. *J. Chem. Soc. Trans.* **1907**, *91*, 2001–2021. [CrossRef]

50. Symth, C. *Dielectric Behaviour and Structure*; McGraw-Hill: New York, NY, USA, 1955.

51. Jonsche, A.K. Relaxation in low-loss dielectrics. *J. Mol. Liq.* **2000**, *87*, 259–268. [CrossRef]

52. Kabasakalian, P.; Kalliney, S.; Westcott, A. Enzymatic Blood Glucose Determination by Colorimetry of N,N-Diethylaniline-4-Aminoantipyrine. *Clin. Chem.* **1974**, *20*, 606–607. [CrossRef] [PubMed]